

1st Year CSI Report: Part 2

Near-fault Ground Motion Prediction, Site Effects and Wave Propagation at Regional Scale for a Shallow Earthquake in Southeast France

PhD student: Hongyi SU^{1,2}

Thesis supervisor: Sébastien HOK¹, Mathieu CAUSSE², Céline GELIS¹,
Cécile CORNOU²

CSI committee: Bertrand DELOUIS³, Céline BEAUVAL²

¹Bureau d’Evaluation des Risques Sismiques pour la Sûreté des Installations (BERSSIN), IRSN,
Fontenay-aux-Roses, France

²Institut des Sciences de la Terre (ISTerre), UGA, Grenoble, France

³Laboratoire Géoazur, Université de la côte d’Azur, France

Key Points:

- Convert overlapping isosceles triangle slip rate functions to dynamic compatible regularized Yoffe slip rate functions.
- Estimate dynamic parameters D_c , $\mu_s - \mu_d$ with assumptions, using scaling relations from Tinti, Fukuyama, et al. (2005).
- Perform dynamic rupture modeling with obtained dynamic parameters and assumed initial stress field.

1 Introduction

Kinematic and dynamic rupture modeling are the two main methods for fault rupture modeling. Kinematic rupture model (KRM) is data-constrained, while dynamic rupture model (DRM) is physics-based. KRM can be quickly computed using existing inversion programs and is typically available soon after an earthquake Tinti et al. (2009). However, KRMs are often non-unique and depend on robust observational data coverage. On the other hand, DRMs based on laboratory experiments and elastodynamic equations, introduce friction and dynamic stress evolution interacting with seismic wave propagation Ramos et al. (2022). By combining these two methods, we can select KRMs that are physics-consistent from multiple solutions and develop DRMs which are data-informed.

Previous work shows dynamic parameters can be extracted from traction-slip curves by solving elastodynamic equations from KRMs. (Tinti, Spudich, & Cocco (2005), Causse et al. (2014)). In this study, we directly extract dynamic parameters from a kinematic

Corresponding author: Hongyi SU, hongyi.su@irsn.fr

model of 2019 Mw 4.9 Le Teil earthquake (by Bertrand Delouis, 2023) using a scaling relation from Tinti, Fukuyama, et al. (2005) without solving elastodynamic equations. As the scaling relations contain parameters from specific regularized Yoffe slip rate functions, we first convert the overlapping isosceles triangle slip rate functions used in kinematic modelling to dynamic consistent regularized Yoffe functions defined by Tinti, Fukuyama, et al. (2005). Then we compute critical slip distance D_c and breakdown stress drop σ_b using the scaling relations. Finally, we perform a dynamic rupture modelling with the code SeisSol (<https://seissol.org/>) using the obtained parameters with necessary assumptions about the initial stress field.

2 Kinematic Model

We use the latest kinematic model of the 2019 Mw 4.9 Le Teil earthquake. Inversion details refer to Bertrand Delouis (2023).

2.1 Fault Geometry

This kinematic model is inverted on a planar fault consists of 60 subfaults. Each subfault is 0.5 km long along strike and dip, covering an area of 0.25 km². There are 12 subfaults along the strike and 5 along the dip, resulting in a total fault length of 6 km and a width of 2.5 km, dipping to the SE at 57 degrees and striking 47 degree to the north. Figure 1 shows the fault geometry, the number in the center of each subfault indicates the moment magnitude of the corresponding subfault. The seismic moment of the entire fault is a partition of seismic moment come from all subfaults. The overall magnitude is Mw 4.95.

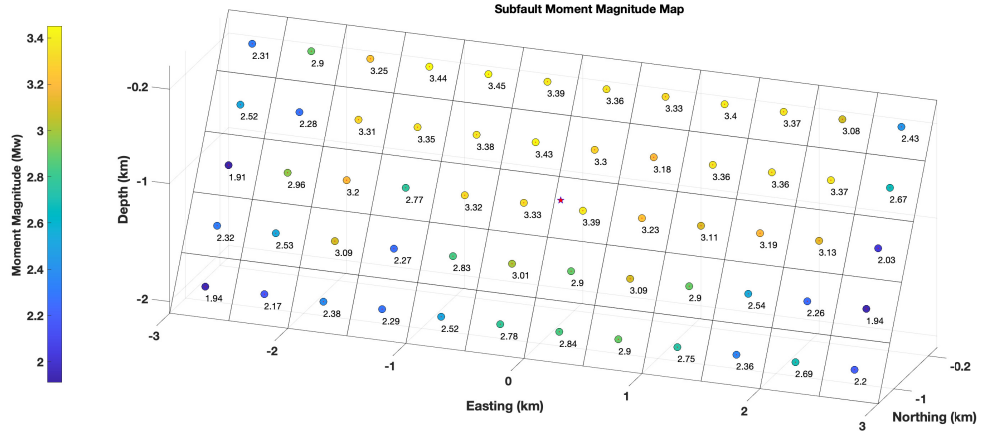


Figure 1: Configuration of the kinematic model. The red star indicates the hypocenter used in dynamic rupture simulations. The fault length is 6 km and fault width is 2.5 km, dip angle is 57 degrees. The colorbar indicates moment magnitude of each subfault.

3 Analysis

3.1 Convert Source Time Functions to Regularized Yoffe Functions

The source time function (STF) used in kinematic modeling consists of three overlapping isosceles triangular functions. Also known as the slip rate function, STF describes how slip evolves over time. At each source point, the slip rate function is constructed using the maximum amplitudes of the three triangular functions with a fixed duration of 0.3 seconds.

We show an example of a constructed slip rate function of a subfault in Figure 2 and its corresponding regularized Yoffe slip rate function in Figure 3, following the formulation by Tinti et al. 2005, Tinti, Fukuyama, et al. (2005). To construct the regularized Yoffe function, only 3 parameters are required, namely T_{acc} , τ_R and D_{max} . T_{acc} is the positive acceleration time, it defines the time when the slip rate reaches the maximum, V_{peak} . τ_R is the total rupture duration; and D_{max} is the final slip. All overlapping isosceles triangular STFs have a duration of 0.6 seconds by definition (ref. Bertrand Delouis).

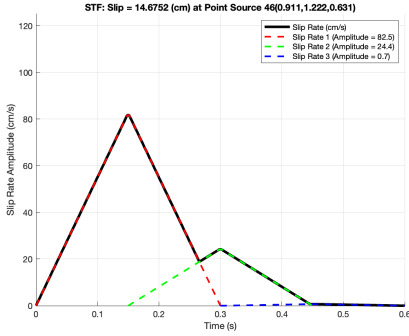


Figure 2: Constructed slip rate function for point source N. 46

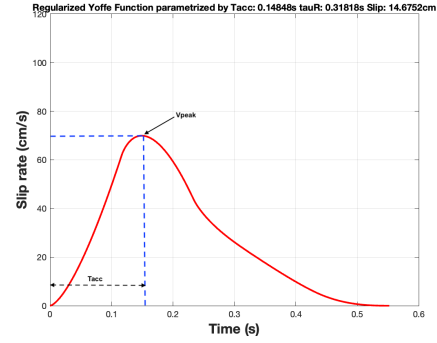


Figure 3: Constructed regularized Yoffe slip rate function for point source N. 46

Figure 4 and 5 show the slip evolution curve, which slip are computed by integrating the area under the slip rate functions. The duration for overlapping isosceles triangle slip rate functions (OITFs) is 0.6s, and the duration for regularized Yoffe slip rate functions (RYFs) is $2 \cdot \tau_s + \tau_R$ due to convolution, where τ_s is T_{acc} divided by 1.27 Tinti, Fukuyama, et al. (2005) Tinti et al. (2021).

Then we vary the input parameter τ_R for the RYFs to better fit the slip curve with the one integrated from OITFs, we calculate the time when the slip reaches 90% of the total slip from the slip evolution of the overlapping isosceles triangle functions (OITFs). Figure 6 show the parameter τ_R decreased from 0.6 s to less than 0.15 s for the point source N. 46. Comparing Figure 7 (slip curve before varying τ_R) to Figure 8 (slip curve after varying τ_R), we see that adjusting τ_R significantly improves the slip evolution fitting between converted Yoffe and original triangle slip rate function.

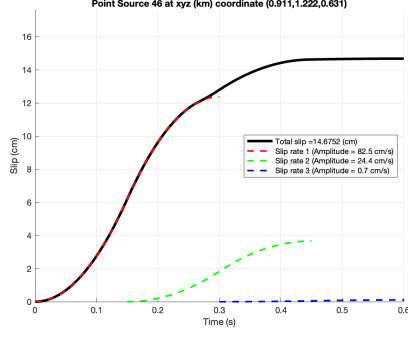


Figure 4: Constructed slip evolution curve for point source N. 46 from OITFs

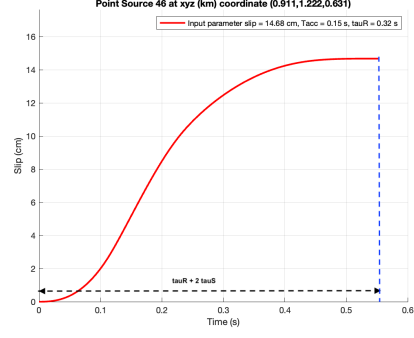


Figure 5: Constructed slip evolution curve for point source N. 46 from RYFs

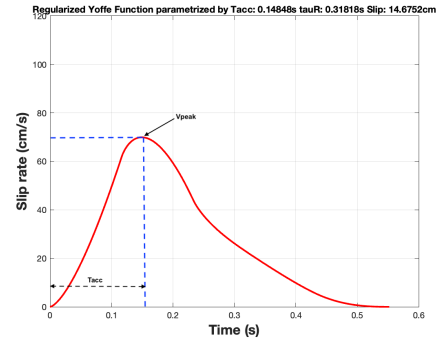
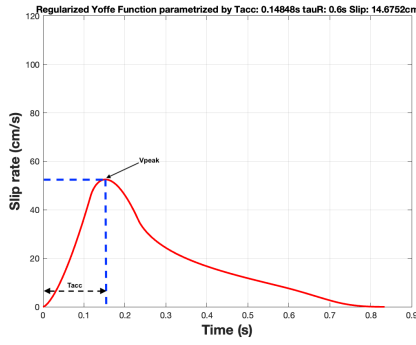


Figure 6: Left: Constructed RYF for point source N. 46 with constant τ_R Right: Constructed RYF for point source N. 46 with heterogeneous τ_R (time when slip reaches 90% of the final slip from the slip evolution curve obtained by OITFs)

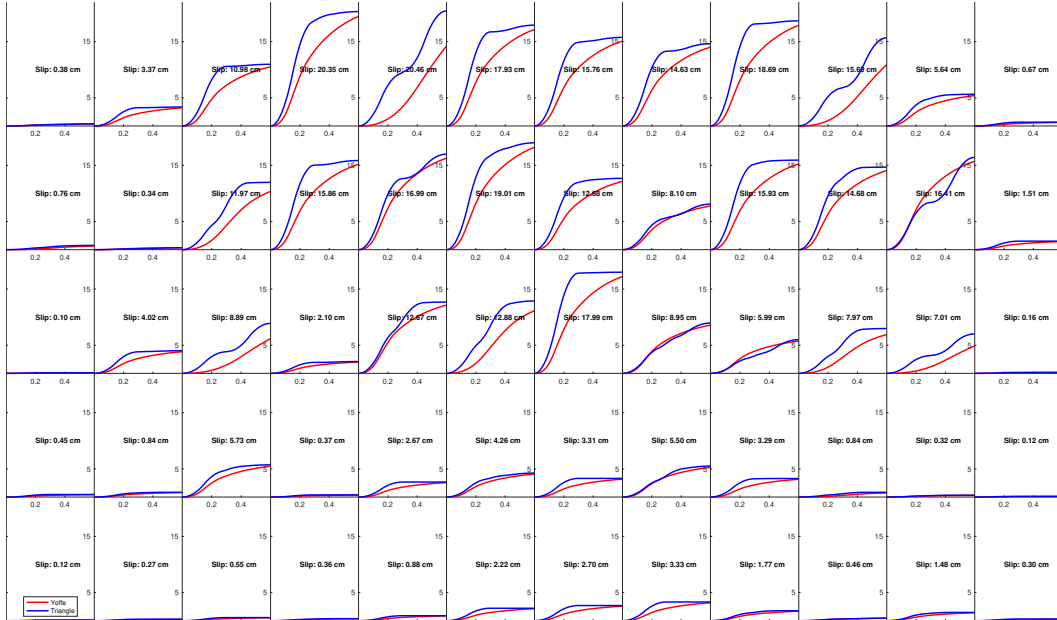


Figure 7: Comparison of slip evolution from the overlapping triangular STF and the converted regularized Yoffe STF before varying τ_R .

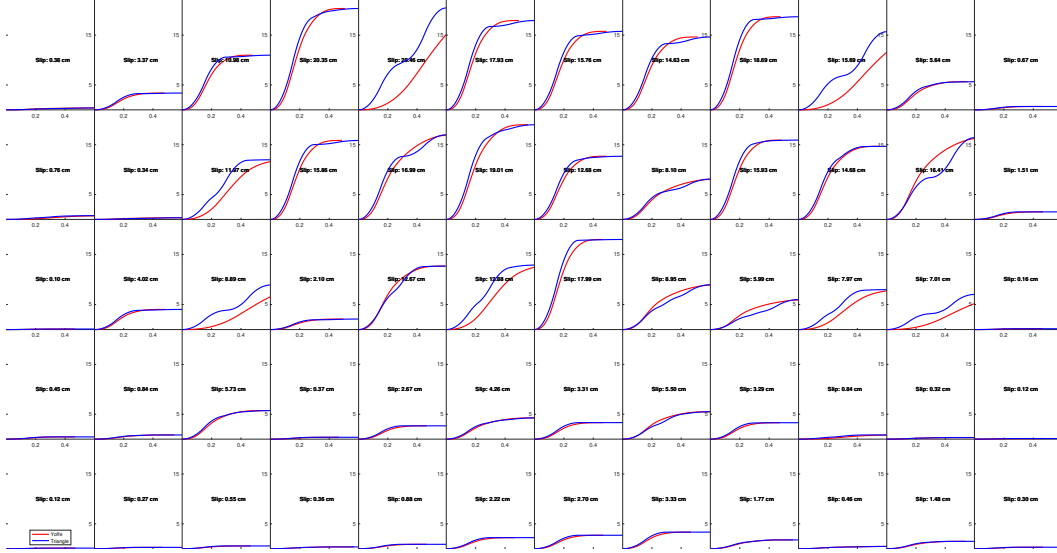


Figure 8: Comparison of slip evolution from the overlapping triangular STF and the converted regularized Yoffe STF after varying τ_R .

3.2 Extract Dynamic Parameters using Scaling Relations

We first extract dynamic parameter, D_c , using the following scaling relation from Tinti, Spudich, & Cocco (2005)

$$D_c \propto \sqrt{\frac{T_{acc}}{\tau_R}} D_{max} \quad (1)$$

we assume a linear scaling factor $C1$ and set $C1 = 1$. then Equation 1 becomes

$$D_c = C1 \sqrt{\frac{T_{acc}}{\tau_R}} D_{max} \quad (2)$$

where D_{max} is the final slip, T_{acc} is the positive acceleration time and τ_R is the rupture duration. Figure 9 shows the computed D_c distribution (interpolated) across the fault plane.

Next, we extract the breakdown stress drop using the following relation from Tinti, Spudich, & Cocco (2005).

$$V_{peak} \propto C(V_r) \Delta \sigma_b \quad (3)$$

Let us assume $C(V_r) = C2 \cdot V_r$, then Equation 3 becomes

$$V_{peak} = C2 \cdot V_r \Delta \sigma_b \quad (4)$$

where V_r is rupture velocity, and because

$$\Delta \sigma_b = \sigma_n (\mu_s - \mu_d) \quad (5)$$

and

$$\sigma_n = \rho(z) g z \quad (6)$$

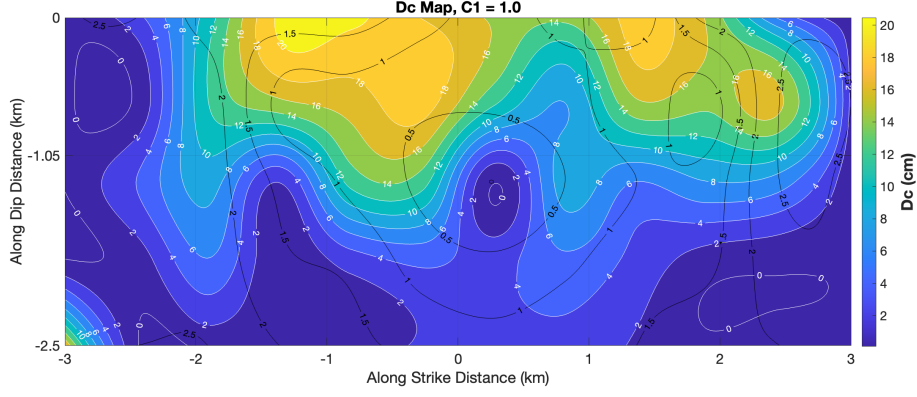


Figure 9: Map of interpolated Dc when $C1 = 1$. The black line contours rupture onset times, and the white line contours the magnitude of Dc

93

Therefore

$$\mu_s - \mu_d = \frac{V_{peak}}{C2 \cdot V_r \rho(z) g z} \quad (7)$$

94

95

96

97

where V_{peak} is one of the parameters for constructing RYFs, and rupture velocity can be computed from the rupture onset time using the method of Pulido & Dalgue (2009), Hok et al. (2011), Figure 10 shows the computed rupture velocity distribution across the fault plane.

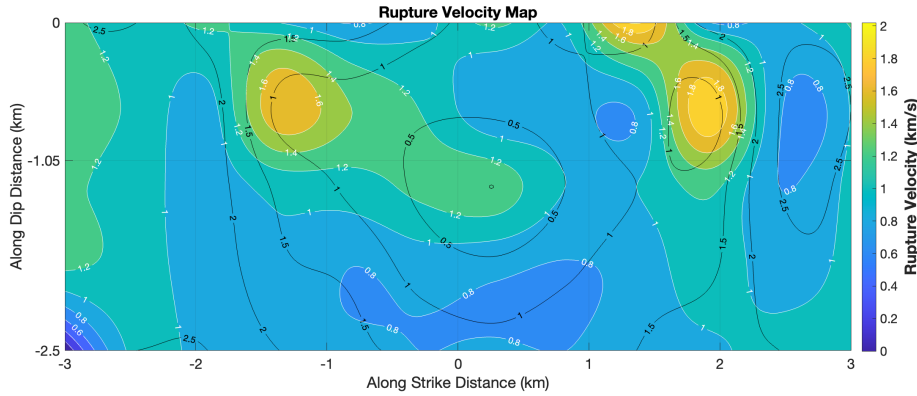


Figure 10: Map of interpolated rupture velocity computed from rupture onset times. the black line contours rupture onset times, and the white line contours the magnitude of rupture velocity.

98

99

100

101

We can tune the parameter C2 to scale the breakdown stress drop, we know from Causse et al. (2021) the stress drop of this event is around $[1 - 2]$ MPa, therefore, we choose $C2 = 2.0e4$, and obtained a reasonable breakdown stress drop across the fault plane, shown in Figure 11

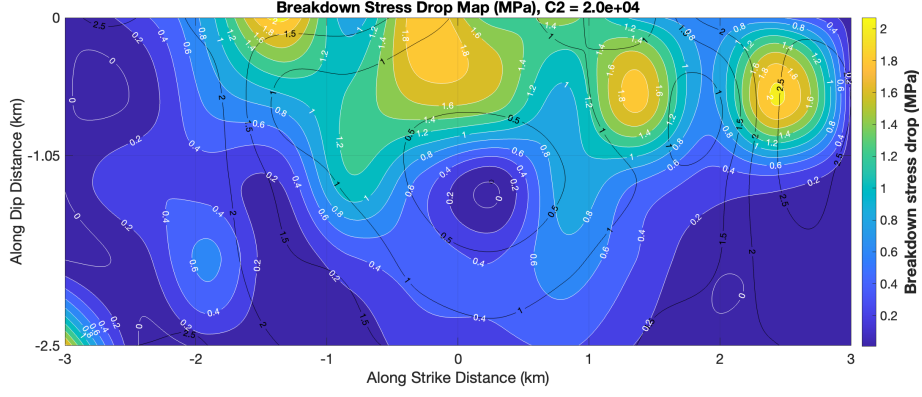


Figure 11: Map of interpolated breakdown stress drop when $C2$ is $2.0e4$. The black line contours rupture onset times, and the white line contours the magnitude of $\Delta\sigma_b$

We can then obtain the dynamic parameter $\mu_s - \mu_d$ by dividing the depth-dependent confining stress. Figure 12 shows $\mu_s - \mu_d$. We use the rheological model from Causse et al. (2021) Causse et al. (2021), detailed in Table 2.

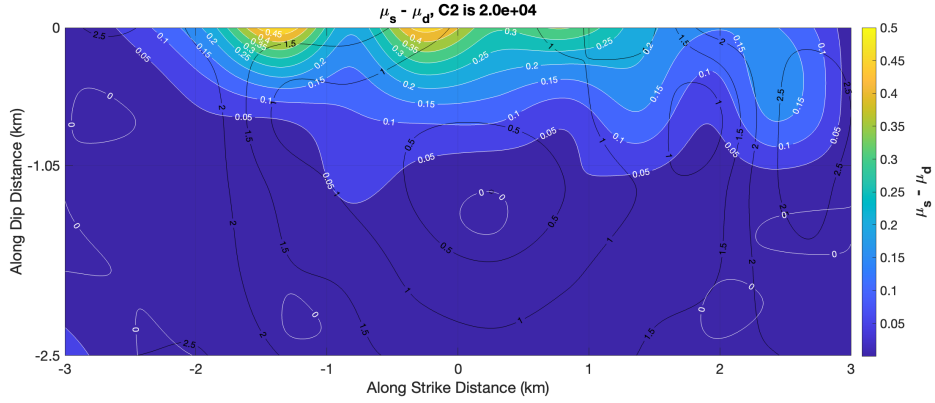


Figure 12: Map of interpolated $\mu_s - \mu_d$ when $C2$ is $2.0e4$. The black line contours rupture onset times, and the white line contours the magnitude of $\mu_s - \mu_d$

Furthermore, Figure 13 shows the computed fracture energy across the fault plane, which defined as:

$$E_G = \frac{1}{2} \cdot \Delta\sigma_b \cdot D_c \quad (8)$$

Having obtained the difference between μ_s and μ_d , we can compute μ_s explicitly by assuming μ_d is constant.

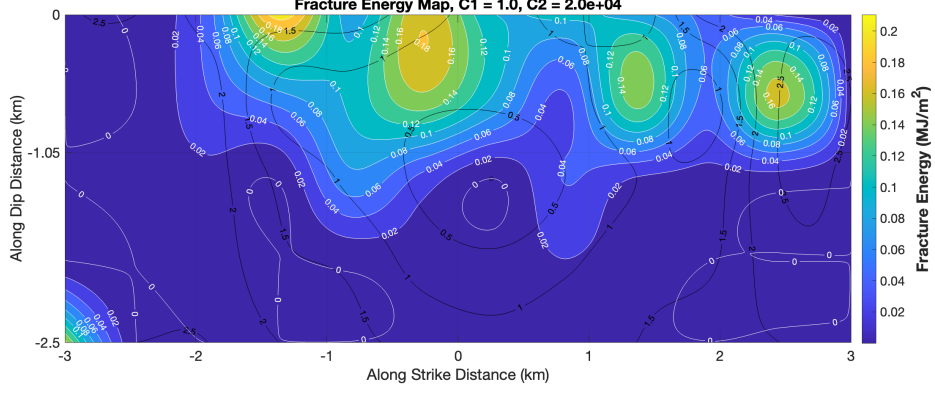


Figure 13: Map of interpolated fracture energy when $C1$ is 1 and $C2$ is 2.0×10^4 . The black line contours rupture onset times, and the white line contours the magnitude of fracture energy

4 Dynamic Simulation

4.1 Assign Parameters using Slip-Weaking Friction

We use slip-weakening friction. With estimated D_c and $\mu_s - \mu_d$ from the scaling relations, we further assume $\mu_d = 0.2$ for all subfaults, and obtain a heterogeneous distribution of μ_s . We also need to assume cohesion is zero for all subfaults.

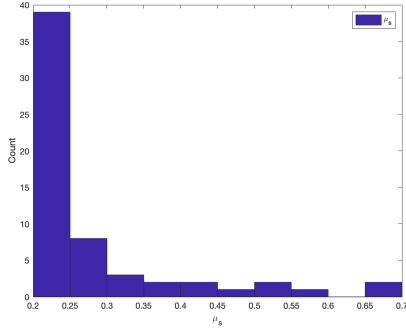


Figure 14: Histogram for input parameter μ_s

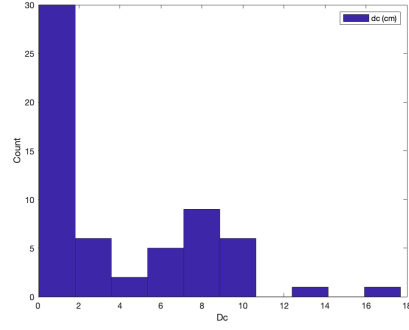


Figure 15: Histogram for input parameter D_c

Figures 14 and 15 show histograms of the input parameters μ_s and D_c , while Figures 16 and 17 display the extract values used for each subfault. From the histogram, we observe that most μ_s values fall below 0.3 and most D_c values are below 2 cm. Upon closer examination, these correspond to subfaults have small slip. A low μ_s indicates a low initial stress level, which is unfavourable for dynamic rupture propagation.

In dynamic rupture modeling (DRM), nucleation is initiated at a single point, i.e. hypocenter, unlike the multiple point sources in inverted kinematic rupture models (KRM), where each point sources are forced to slip without considering dynamic stress evolution.

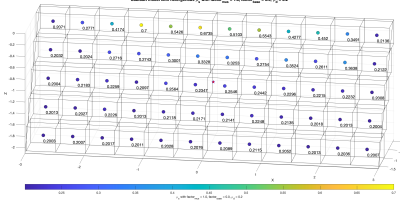


Figure 16: Distribution of input parameter μ_s in each subfault

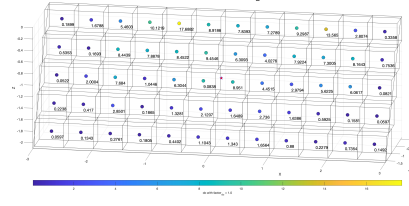


Figure 17: Distribution of input parameter Dc in each subfault

Therefore, adjustments to these subfaults with low μ_s are necessary to sustain the rupture from the nucleation zone and guide the rupture propagates to more favorable subfaults near the surface.

4.2 Setup Initial Stress

Since SeisSol is built with the EASI library (Carsten Uphoff, 2018), we set up the initial stress using a pre-compiled function called **AndersonStress**, which is based on the Mohr-Coulomb failure criteria and Anderson's theory of faulting. The input parameters for **AndersonStress** is listed in Table 1.

Table 1: Stress Parameters in the easi function

Symbol	Meaning
μ_s	static friction coefficients
μ_d	dynamic friction coefficients
SH_{max}	azimuth of the maximum horizontal compressive stress
S_v	indicates which principal stress is vertical
c	cohesion
ν	the stress shape ratio
S	S-parameter
sig_{zz}	effective confining pressure

μ_s is heterogeneous, we estimated μ_s from the scaling relations, the value is displayed in Figure 16. μ_d is homogeneous and assumed equal to 0.2. SH_{max} is homogeneous and we use a constant value of 0, this parameter is the same as the horizontal projection of the largest subhorizontal stress when the stress state is Aberdonian Ulrich et al. (2019) Lund & Townend (2007). S_v is 3 for reverse faulting mechanisms. Cohesion is set to 0 for simplicity. ν describes the ratio between the three principal stresses, and we use a constant value $\nu = 0.5$. S is the ratio between stress excess ($\tau_p - \tau_0$) and dynamic stress drop ($\tau_0 - \tau_r$) Andrews (1976), Previous studies show S-parameter controls the rupture potential on a fault Andrews (1976) Das & Aki (1977), positive and small value promote rupture, large or negative value prevent rupture Aochi & Tsuda (2023), recent studies also show S-parameter influences rupture style Gabriel et al. (2012), therefore, we can modify this parameter to develop a desired rupture scenario via the initial stress, but in the current setup, we assume S is constant and equal to 0.5. σ_{zz} is depth-dependent and is approximated as $\rho \cdot g \cdot z$. The rheological model used for calculating the effective confining stress is summarized in Table 2.

The function outputs a rank-2 stress tensor at each mesh grid point. Rank-2 tensors are typically represented as matrices. The corresponding stress matrix is symmetric and is parameterized by 6 components.

$$\begin{bmatrix} b_{xx} & b_{xy} & b_{xz} \\ & b_{yy} & b_{yz} \\ & & b_{zz} \end{bmatrix}$$

By rotating the stress tensor, we can find the three principal stresses ($s_1 > s_2 > s_3$), where the shear stress is zero.

$$\begin{bmatrix} s_1 & & \\ & s_2 & \\ & & s_3 \end{bmatrix}$$

Conversely, we can compute the 6 stress tensor components from the principal stresses. We prefer using principal stresses because they are directly related to the Mohr-Coulomb circle.

Anderson's theory of faulting assumes that one of the principal stresses is vertical. For reverse faulting focal mechanisms, S_3 is vertical, and S_1 is the maximum horizontal stress, perpendicular to S_3 , as shown in Figure 18.

We demonstrate below how principal stresses are calculated theoretically using the input parameters listed in Table 1 based on the Mohr-Coulomb failure theory.

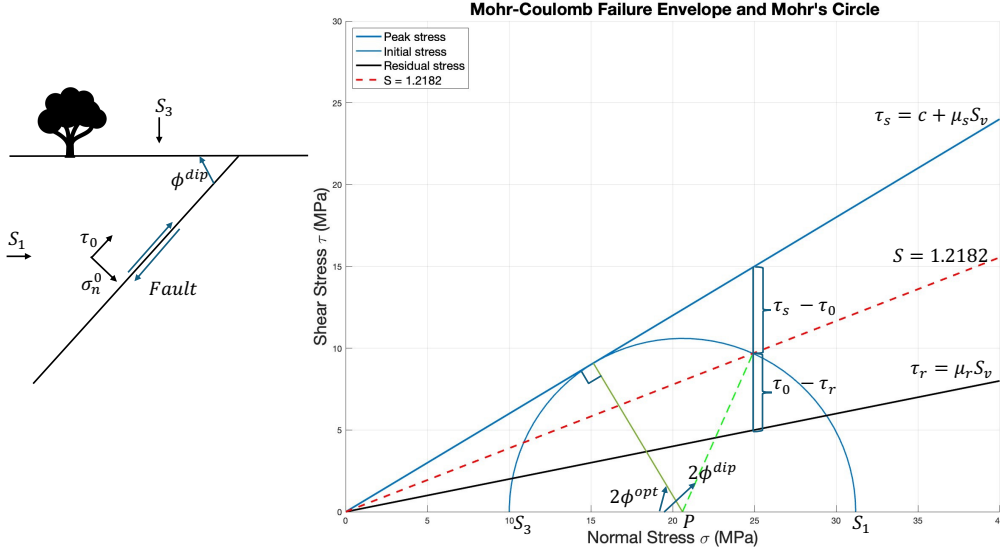


Figure 18: Left: Cross-section of the fault, showing the reverse faulting mechanism, where ϕ^{dip} is the dip angle. Right: Mohr-Coulomb circle illustrating the initial stress state for all possible orientations. The intersection of the green line with the circle represents the initial stress state on an optimally oriented fault, while the intersection of the dashed green line with the circle corresponds to the stress state on a fault with a dip angle of 57° .

In Figure 18, ϕ^{opt} is the optimal angle, μ_s is the static friction coefficient, P is the locus of the optimally oriented Mohr's circle, and ds is the radius of the optimally oriented Mohr's circle. The difference between the maximum and minimum principal stresses is twice ds :

$$\phi^{opt} = \frac{\pi}{4} - \frac{1}{2} \arctan(\mu_s) \quad (9)$$

$$ds = \frac{1}{2}(S_1 - S_3) \quad (10)$$

$$P = \frac{1}{2}(S_1 + S_3) \quad (11)$$

ν is the ratio between 3 principal stresses, $\nu = \frac{s_2 - s_3}{s_1 - s_3}$, therefore,

$$\begin{cases} S_1 = P + ds \\ S_2 = P - ds + 2 \cdot \nu \cdot ds \\ S_3 = P - ds \end{cases} \quad (12)$$

The effective confining stress is,

$$\sigma_{eff} = \frac{S_1 + S_2 + S_3}{3} = P + \frac{(2 \cdot \nu - 1) \cdot ds}{3} \approx \rho \cdot g \cdot z \quad (13)$$

We find initial stress state for optimal angle ϕ^{opt} as:

$$\tau_{0,opt} = ds \cdot \sin(2 \cdot \phi^{opt}) \quad (14)$$

$$\sigma_{n,opt}^0 = P - ds \cdot \cos(2 \cdot \phi^{opt}) \quad (15)$$

In Figure 18, blue line is peak stress and black line is residual stress, c is cohesion, μ_d is dynamic friction coefficient,

$$\tau_{p,opt} = c + \mu_s \cdot \sigma_{n,opt}^0 \quad (16)$$

$$\tau_{r,opt} = \mu_d \cdot \sigma_{n,opt}^0 \quad (17)$$

Relative fault strength R is the ratio of the static stress drop ($\tau_0 - \tau_r$) to the breakdown stress drop ($\tau_p - \tau_r$) (T in Aochi & Ulrich, 2015 Aochi & Ulrich (2015)).

$$R_{opt} = \frac{1}{1 + S_{opt}} = \frac{\tau_{0,opt} - \tau_{r,opt}}{\tau_{p,opt} - \tau_{r,opt}} \quad (18)$$

From Equation 18, 13, 14, and 15

$$\begin{cases} ds = \frac{R_{opt} \cdot c + \sigma_{eff} \cdot A}{\sin(2\phi^{opt}) + \cos(2\phi^{opt}) \cdot A + \alpha \cdot A} \\ A = R_{opt} \cdot (\mu_s - \mu_d) + \mu_d \\ \alpha = \frac{2 \cdot \nu - 1}{3} \end{cases} \quad (19)$$

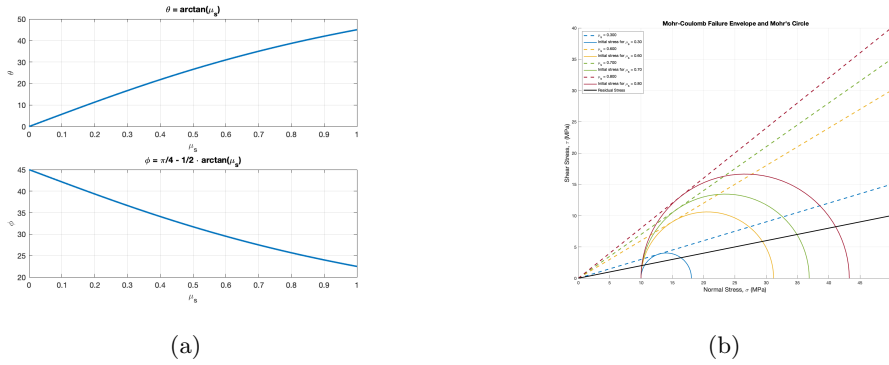
Similarly, we find initial stress state for dip angle ϕ^{dip} as:

$$\begin{cases} \tau_{0,dip} = ds \cdot \sin(2 \cdot \phi^{dip}) \\ \sigma_{n,dip}^0 = P - ds \cdot \cos(2 \cdot \phi^{dip}) \\ \tau_{p,dip} = c + \mu_s \cdot \sigma_{n,dip}^0 \\ \tau_{r,dip} = \mu_d \cdot \sigma_{n,dip}^0 \\ R_{dip} = \frac{1}{1+S_{dip}} = \frac{\tau_{0,dip} - \tau_{r,dip}}{\tau_{p,dip} - \tau_{r,dip}} \end{cases} \quad (20)$$

Le Teil rheological model (Causse et al., 2021)							
depth [km]	0.0	0.63	1.2	1.42	2.03	2.19	5.96
ρ [kg/m ³]	2407	2688	2165	2465	2470	2667	2685
V_s [m/s]	2047	3645	1200	2291	2314	3457	3616

Table 2

Higher μ_s results in greater absolute initial normal and shear stresses (larger circle) when the S parameter is fixed. Figure 19 (a) shows how the optimally oriented angle ϕ varies with changes in μ_s . We observe that μ_s is highly sensitive to ϕ ; a small change in ϕ can lead to a significant change in μ_s . This sensitivity is challenging because we lack precise information about ϕ i.e. the dip angle from the kinematic inversion, which is a not well-constrained parameter Delouis et al. (2021). For example, Aochi and Tsuda's simulation used a dip angle of 50 degrees Aochi & Tsuda (2023), resulting in a much higher stress level and a more favorable S parameter compared to the 57 degrees used in this setup. Figure 19 (b) illustrates that a higher μ_s results in a much larger Mohr's circle and therefore higher absolute stress.

Figure 19: (a) ϕ and θ as a function of μ_s (b) Mohr's circle for different μ_s

4.2.1 Initial Stress

The computed initial stress field for each subfault is shown in Figures 23 and 21. We display only the initial shear stress in the dip direction since SH_{\max} is assumed to

be 0, resulting in negligible shear stress in the strike direction. To sustain dynamic rupture, we increase absolute initial stress by adding 0.2 in μ_s to the subfaults in the upper central part using a test-and-trial approach.

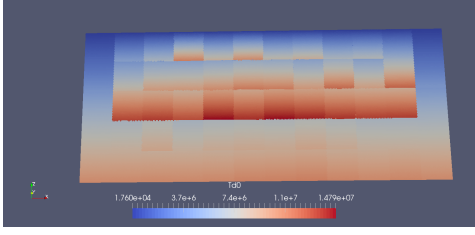


Figure 20: Td0

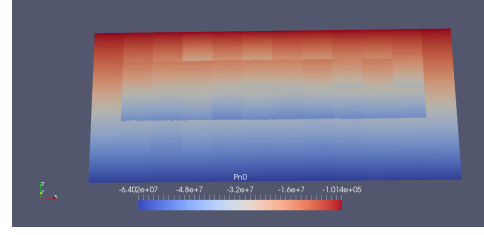


Figure 21: Pn0

4.3 Nucleation

We adopted the weak nucleation method following Tinti et al. (2021). This method is considered superior to the overstressing method, which often results in artificially large fault slip in the hypocentral area and creates unrealistic strong pulses in synthetic seismograms, as noted in Palgunadi et al. (2020). The weak nucleation method gradually reduces the yield strength within an elliptical area centered at the hypocenter. This area expands over time at a decreasing rate, as described in Harris et al. (2018). This approach ensures a smooth transition to fully spontaneous dynamic rupture propagation. In our models, the forced nucleation phase lasts less than 1.67 seconds with minimal moment release, using a nucleation initial forcing speed of 300 m/s and a nucleation radius of 0.5 km.

4.4 Dynamic Rupture Results

Figures 23 and 24 show the assumed initial shear stress, which is the same as in the previous section, except for a manual reduction in fault strength μ_s of subfault No. 43 (see Figure 22). Figure 25 presents the dynamic rupture results for setup 13, including shear stress drop in the dip direction (T_d), absolute shear stress along dip (Td0), slip rate in dip direction (m/s), and absolute slip (m), from top to bottom panels at each simulation time. The shear stress drop is negative within the rupture front, except for the subfault where we reduced μ_s . This subfault has lower stress levels, slowing rupture propagation. After the rupture gains sufficient energy from subfaults on the right side, between 7 to 8 seconds, it continues to the left side.

Figure 26 (a) shows the source time function of the dynamic rupture model. The blue line shows the target kinematic model source time function, the time of two models shown are shifted for better visual comparison. Figure 26 (b) shows the Fourier spectra of the corresponding source time functions, both models start to decay at around 1 Hz, the dynamic rupture model has higher amplitude but similar decaying slope compare to the kinematic model.

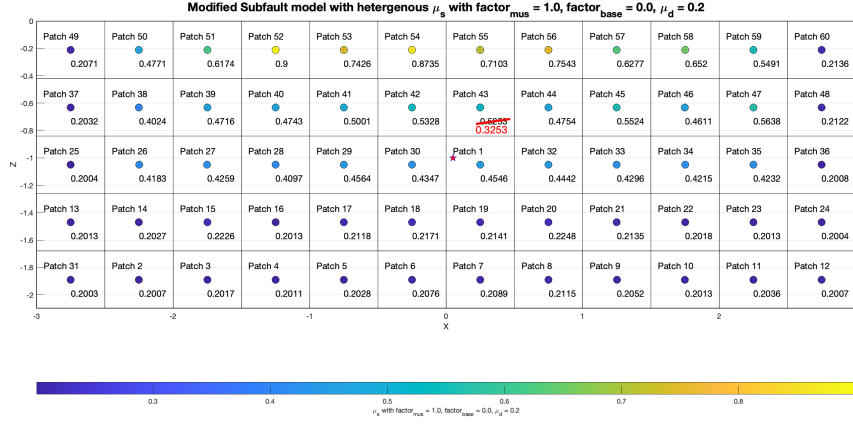


Figure 22: Modified μ_s distribution, setup 13

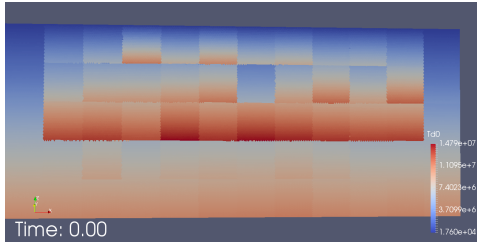


Figure 23: Td0 setup13

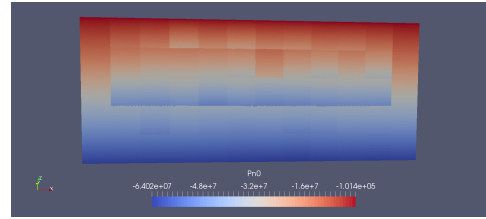


Figure 24: Pn0 setup13

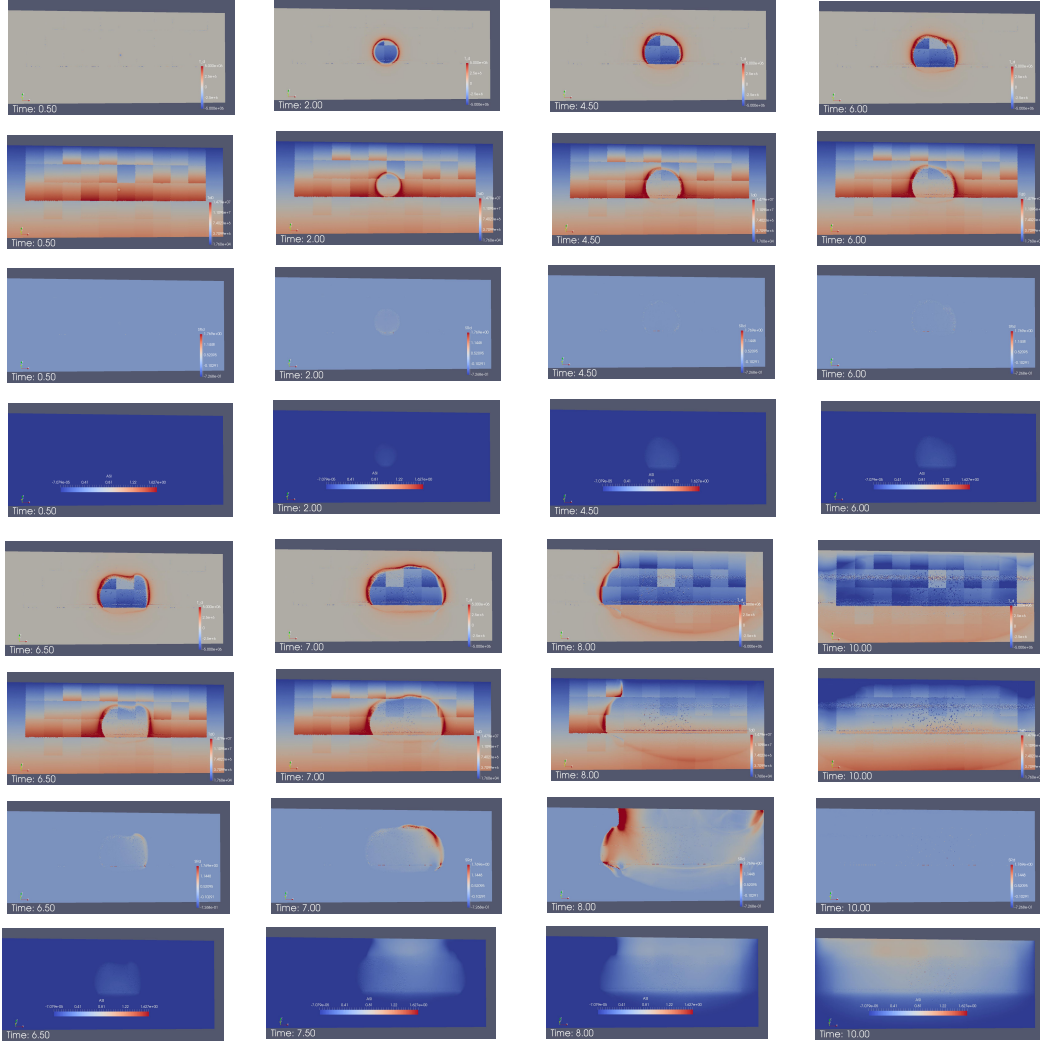


Figure 25: Rupture dynamics for setup13 from 0 to 10 s, T_d is shear stress drop (Pa) in dip direction, T_{d0} is the absolute shear stress (Pa) along dip, SRD is the slip rate (m/s) in dip direction, and ASI is absolute slip (m),

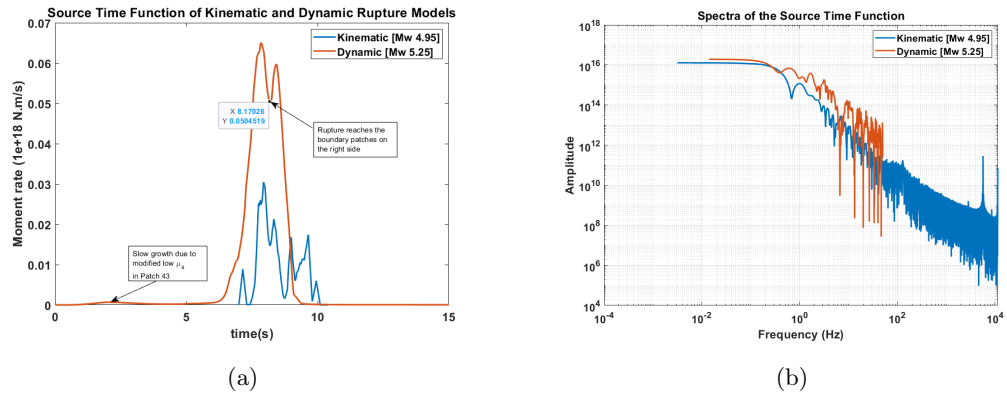


Figure 26: Source time function and its spectra of dynamic rupture model and target kinematic rupture model with notations

4.5 Application

This model demonstrates that dynamic rupture history can be guided by assigning specific dynamic parameters to each subfault.

We can also justify the modifications, For example, the decrease of μ_s could be explained by fluid from heavy rainfall penetrating 1km depth and weakening the surrounding rocks.

This method demonstrates the ability to control and modify dynamic rupture evolution through assigned dynamic parameters, In the next, we need to test more setups and develop a model that is compatible with the kinematic model in terms of moment magnitude, final slip distribution, rupture history, rupture velocity, and stress drop. However, we should point out that we might not be able to satisfy all criteria in a single dynamic rupture model, but we can hope for finding conditions that is necessary for achieving each criterion.

References

- Andrews, D. (1976). Rupture propagation with finite stress in antiplane strain. *Journal of Geophysical Research*, 81(20), 3575–3582.
- Aochi, H., & Tsuda, K. (2023). Dynamic rupture simulations based on depth-dependent stress accumulation. *Geophysical Journal International*, 233(1), 182–194.
- Aochi, H., & Ulrich, T. (2015). A probable earthquake scenario near istanbul determined from dynamic simulations. *Bulletin of the Seismological Society of America*, 105(3), 1468–1475.
- Causse, M., Cornou, C., Maufroy, E., Grasso, J.-R., Baillet, L., & El Haber, E. (2021). Exceptional ground motion during the shallow mw 4.9 2019 le teil earthquake, france. *Communications Earth & Environment*, 2(1), 14.
- Causse, M., Dalguer, L., & Mai, P. M. (2014). Variability of dynamic source parameters inferred from kinematic models of past earthquakes. *Geophysical Journal International*, 196(3), 1754–1769.
- Das, S., & Aki, K. (1977). A numerical study of two-dimensional spontaneous rupture propagation. *Geophysical journal international*, 50(3), 643–668.
- Delouis, B., Oral, E., Menager, M., Ampuero, J.-P., Trilla, A. G., Régnier, M., & Deschamps, A. (2021). Constraining the point source parameters of the 11 november 2019 mw 4.9 le teil earthquake using multiple relocation approaches, first motion and full waveform inversions. *Comptes Rendus. Géoscience*, 353(S1), 1–24.
- Gabriel, A.-A., Ampuero, J.-P., Dalguer, L., & Mai, P. M. (2012). The transition of dynamic rupture styles in elastic media under velocity-weakening friction. *Journal of Geophysical Research: Solid Earth*, 117(B9).
- Harris, R. A., Barall, M., Aagaard, B., Ma, S., Roten, D., Olsen, K., ... others (2018). A suite of exercises for verifying dynamic earthquake rupture codes. *Seismological Research Letters*, 89(3), 1146–1162.
- Hok, S., Fukuyama, E., & Hashimoto, C. (2011). Dynamic rupture scenarios of anticipated nankai-tonankai earthquakes, southwest japan. *Journal of Geophysical Research: Solid Earth*, 116(B12).
- Lund, B., & Townend, J. (2007). Calculating horizontal stress orientations with full or partial knowledge of the tectonic stress tensor. *Geophysical Journal International*, 170(3), 1328–1335.
- Palgunadi, K. H., Gabriel, A.-A., Ulrich, T., López-Comino, J. Á., & Mai, P. M. (2020). Dynamic fault interaction during a fluid-injection-induced earthquake: The 2017 m w 5.5 pohang event. *Bulletin of the Seismological Society of America*, 110(5), 2328–2349.
- Pulido, N., & Dalguer, L. A. (2009). Estimation of the high-frequency radiation of the 2000 tottori (japan) earthquake based on a dynamic model of fault rupture: Application to the strong ground motion simulation. *Bulletin of the Seismological Society of America*, 99(4), 2305–2322.
- Ramos, M. D., Thakur, P., Huang, Y., Harris, R. A., & Ryan, K. J. (2022). Working with dynamic earthquake rupture models: A practical guide. *Seismological Society of America*, 93(4), 2096–2110.
- Tinti, E., Casarotti, E., Ulrich, T., Taufiqurrhman, T., Li, D., & Gabriel, A.-A. (2021). Constraining families of dynamic models using geological, geodetic and strong ground motion data: The mw 6.5, october 30th, 2016, norcia earthquake, italy. *Earth and Planetary Science Letters*, 576, 117237.
- Tinti, E., Cocco, M., Fukuyama, E., & Piatanesi, A. (2009). Dependence of slip weakening distance (d c) on final slip during dynamic rupture of earthquakes. *Geophysical Journal International*, 177(3), 1205–1220.
- Tinti, E., Fukuyama, E., Piatanesi, A., & Cocco, M. (2005). A kinematic source-

- 281 time function compatible with earthquake dynamics. *Bulletin of the Seismological*
 282 *Society of America*, 95(4), 1211–1223.
- 283 Tinti, E., Spudich, P., & Cocco, M. (2005). Earthquake fracture energy inferred
 284 from kinematic rupture models on extended faults. *Journal of Geophysical Re-*
 285 *search: Solid Earth*, 110(B12).
- 286 Ulrich, T., Gabriel, A.-A., Ampuero, J.-P., & Xu, W. (2019). Dynamic viability of
 287 the 2016 mw 7.8 kaikōura earthquake cascade on weak crustal faults. *Nature com-*
 288 *munications*, 10(1), 1213.